Visualizing percolation and ion transport in hybrid solid electrolytes for Li-metal batteries

Wahid Zaman[a], Nicholas Hortance[b], Marm B. Dixit[a], Vincent De Andrade[c] and Kelsey B. Hatzell[a,b,d]

[a]Department of Mechanical Engineering, Vanderbilt University, Nashville, TN 37240, USA. E-mail: kelsey.b.hatzell@vanderbilt.edu
[b]Interdisciplinary Department of Material Science, Vanderbilt University, Nashville, TN 37240, USA
[c]Advanced Photon Source, X-ray Science Division, Argonne National Laboratory, 9700 South Cass Avenue, Argonne, IL 60439-4837, USA
[d]Department of Chemical and Biomolecular Engineering, Vanderbilt University, Nashville, TN 37240, USA

Abstract

Hybrid solid electrolytes are composed of organic (polymer) and inorganic (ceramic) ion conducting materials, and are promising options for large-scale production of solid state lithium metal batteries. Hybrid solid electrolytes containing 15 vol% Al-LLZO demonstrate optimal ionic conductivity properties. Ionic conductivity is shown to decrease at high inorganic loadings. This optimum is most obvious above the melting temperature of polyethylene oxide where the polymer is amorphous. Structural analysis using sychrotron nanotomography reveals that the inorganic particles are highly aggregated. The aggregation size grows with inorganic content and the largest percolating clusters measured for 5 vol%, 15 vol% and 50 vol% were _12 mm3, 206 mm3, and 324 mm3, respectively. Enhanced transport in hybrid electrolytes is shown to be due to polymerjparticle (Al-LLZO) interactions and ionic conductivity is directly related to the accessible surface area of the inorganic particles within the electrolyte. Ordered and well-dispersed structures are ideal for next generation hybrid solid electrolytes.

1 Introduction

Solid state electrolytes that can suppress lithium dendrite growth are potential candidates for energy dense metallic lithium batteries 1–3. Currently, there are several solid electrolytes that exist and broadly fall into two material categories: (1) organic and (2) inorganic. Polymer electrolytes are advantageous because they can be manufactured easily into thin films, are mechanically robust, and flexible4,5. However, polymer electrolytes have lower ionic conductivities when compared with their ceramic counterpart. Ceramic conductors boast outstanding ionic conductivities (_10 mS/cm) but processing the electrolyte into thin films (50-100mm) for efficient device integration still remains a challenge because of the brittle nature of the ceramic6. A hybrid approach which combines a polymer and ceramic into a composite electrolyte is one potential route toward achieving both efficient transport and processability in all solid state batteries 7–10. A hybrid or composite solid electrolyte is composed of an ion conducting organic polymer and an inorganic material (i.e. SiO2, Al2O3, etc.). The addition of an 'inactive' inorganic (composite) 7,11 or ion conducting glass/ceramic (hybrid)12 increases the electrolyte's elastic modulus and critical current density13–15. The role of the inorganic constituent on ionic transport is unresolved in hybrid electrolytes. Some reports suggest that the addition of an 'inactive' ceramic can increase the ionic conductivity of the electrolyte by four orders of magnitude7,11. However, in water-free environments, and with different inorganic materials, this improvement is less obvious16 and can even decrease17–19 with increasing inorganic loading. Prior reports suggest that the the nature of lithium transport in composite systems is fundamentally related to constituent interactions (i.e. polymerjceramic)7,8,10,20. In composite electrolytes with inert fillers,

the nature of surface interactions and confinement can dictate transport 21,22. Inorganic compounds that are acidic or neutral are more likely to form hydrogen bonding with the salt anions and the oxygen in the polyethylene oxide. This bonding, can potentially promote efficient salt dissociation and faster Li+ ion transport 7. Furthermore, the addition of an inert filler can control the crystallization kinetics of polyethylene oxide and enable a greater concentrations of highly conducting
amorphous domains20. However, if the polymer (ion conducting phase) is diluted too much with fillers (non ion conducting phase), these positive impacts are negated. At high filler content the dilution effect predominates and the ionic conductivity decreases. Thus, in composite electrolytes, optimal filler concentration between 8-20 vol% are reported7,20. While dilution theory explains the decrease in ionic conductivity at high filler loadings in composite electrolytes, it cannot completely explain the same trend observed in hybrid electrolytes. The fillers in hybrid electrolytes are active (i.e. ion conducting) and thus there should not be a decrease in ionic conductivity at high loadings. Furthermore, the inorganic ion conductor typically has a higher ionic conductivity than the polymer electrolyte (especially at low temperatures) and thus it is counterintuitive that more inorganic ion conductors would lead to decreased transport properties. The decrease in ionic conductivity at high inorganic content loading (>30 vol%) is often attributed to a formed interfacial resistance (Rint) at the polymerjceramic interface 10,19,23 which prevents transport between the two materials. Many reports suggest that this interfacial region is the dominant path for ion transport in a hybrid electrolyte due to the formation of a space charge layer 24. Prior reports have used indirect techniques such as NMR, modeling, and electrochemical techniques to probe the origin of this surface-driven transport mechanism25,26. Herein, we intend to directly evaluate this hypothesis via a detailed nano-structural analysis of hybrid solid electrolytes. Ultimately, the underlying structure of the inorganic phase within the polymer matrix is shown to be a significant descriptor for transport properties.

2 Experimental

2.1 Solid electrolyte synthesis, processing and characterization

Lithium lanthanum zirconium oxide (Li7:5La3Zr2Al0:25O12) or Al-LLZO was synthesized using a conventional solid-state approach. Stoichiometric ratio of LiOH (pre-dried at 200_C under vacuum for 6 hours), La2O3 (pre-dried at 1200_C for 12 hours), ZrO2, and Al2O3 was dispersed in isopropanol and ball milled in a planetary ball mill (Fritsch, Pulverisette 7 premium line) at 500 RPM (4 hours). Milling cycles included 5 minutes of milling and 15 minutes of rest. Powders were calcined in alumina boat at 900_C for 10 hours. A second ball mill step (500 RPM) for 2 hours was carried out for size reduction. A series hybrid electrolytes were prepared via adding Al-LLZO (5-50 vol%) to a solution of polyethylene oxide (PEO) and lithium perchlorate (LiClO4) in acetonitrile. The molar ratio of ethylene oxide (EO) and Li+ was 18:1. The composite ink was ball milled for an hour to ensure effective mixing and further processed via tape-casting to produce
free-standing films. After drying under vacuum for 10 hours, the films were peeled off from the substrate. Films had an average thickness around 60-70 mm. Electrolytes contained 5 vol% (16.6 wt%), 10 vol% (29.6 wt%), 15 vol% (40.1 wt%), 25 vol% (55.9 wt%), or 50 vol% (79.1 wt%) of Al-LLZO. The LLZO:PEO-LiClO4 composition was calculated assuming the density of PEO, LiClO4 and LLZO were 1.21 g/cm3, 2.42 g/cm3 and 5.2 g/cm3, respectively. X-ray diffraction (XRD) on neat LLZO and PEO-LLZO electrolytes was carried on by using Rigaku Smart Lab (Cu Ka Xray).
The diffraction patterns were taken from 10_-60_ with a step size of 0.01_(Fig. S1a) Thermal stability of the electrolytes was analyzed by thermogravitimetric analysis (TGA) on Instrument Specialist's TGA-1000. Thermal degradation of the materials was carried out from 25_ to 900_C at 20_C heating rate (Fig. S1b) .

2.2 Synchrotron Nanotomography

The Synchrotron X-ray Nanotomography was carried out at beamline 32-ID-C of Advanced Photon Source, Argonne National Laboratory27. Filtered monochromatic X-rays at 8 keV were used for imaging. The X-ray beam was focused on the sample using a pinhole and condenser upstream of the sample. X-rays transmitted through the sample are focused on the detector through a Fresnel zone plate and phase ring (Fig. S2). A 2448 _ 2048 pixel area detector was used that provided a field of view of 73.2 x 61.2 mm and a resolution of 50 nm was obtained after binning. A small triangular piece was cut off from the membrane and glued on the tip of a metal pin with epoxy. The protruding tip of the sample was imaged. All samples were exposed to X-rays for one hour prior to imaging to stabilize the polymer and ceramic phases. 1201 projections were collected over 180_ rotation of the sample with an exposure time of 300 ms. The total run time for a single tomography scan was _6 minutes. Simultaneous Iterative Reconstruction Technique (SIRT) algorithm within the ASTRA toolbox was used for reconstructing the tomography data28–30. 200 iterations of the algorithm was found to produce the best quality images and was used for all reconstructions. Subsequent image processing and segmentation routines were carried out in ImageJ31.

2.3 Transport Measurements

Total Li+ ion transference number of PEO-LLZO membranes was carried out by using AC impedance and DC polarization method. After assembling the membranes in symmetric LijPEO-LLZOjLi cells, a stepped voltage of 10mV was applied and the current was recorded as a function of time. The cells were thermally treated from 20°C to 90°C three times for a time period of 45 minutes before proceeding with the electrochemical analysis. Transference number t_{Li+} was calculated as:

$$t_{Li^+} = \frac{I_s(V - I_o R_o)}{I_o(V - I_s R_s)}, \qquad (1)$$

where *V* is the applied voltage, *I*0 is the initial current at the beginning of the chronoamperometry step and *I*S is the steady state current. *R*0 and *R*s are the initial and steady state resistances extracted from electrochemical impedance spectroscopy. Ionic conductivity was measured via directly casting the electrolyte on to copper foil blocking electrodes. All samples were hot pressed at 50°C for an hour prior to the measurement. Electrochemical impedance spectroscopy (1 MHZ and 100 mHz) was run on the samples for operating temperatures between 25°C to 70°C. Activation energy were estimated using the Arrhenius equation.

3 Model Descriptions

A continuum percolation model was built to predict structure driven properties in hybrid solid electrolytes 32,33. This model is based on the heterogeneous distribution of inert fillers dispersed within a matrix where three components are present with different conductivity; insulating fillers, normally conducting dispersing medium and a highly conducting interface region. Al-LLZO has an order of magnitude higher ionic conductivity compared to the polymer matrix. However, the hybrid electrolytes do not exhibit conductivities similar to that of the ceramic particles even at very high loadings. Furthermore, the optimum value of solid loading is found at 15 vol.% which is relatively very small mass fraction of the system. Thus, an assumption of non-conducting filler particles has been made for the purpose of model development. The interfacial layer thickness and conductivity depends on particle size and volumetric loading34. The conductivity calculation is based on effective medium approximation (EMA), which gives a better accuracy in 3-dimensional cases like this. Here, a spherical random void model of dispersion is considered. The domain is a polymer matrix surrounding ion conducting particles with radius *R*. The three well-defined regions are: (1) the ceramic particle snp,

(2) the bulk polymer sp, and (3) the interfacial layer si. The interfacial layers is typically 2-3_ the diameter of the particle and is represented by a thickness of l (nm) in the proposed model. Considering an insulator-interphase model, we assume the grain boundary resistances are large, and thus ion conduction does not occur through the inorganic particle (i.e. snp=0) and that the interphase region is comparable to the size of the inorganic particles (i.e. 200 nm). The ratio between the inorganic particle and interfacial layer to the the inorganic layer is:

$$\eta = \frac{R+\lambda}{R}$$

and the the volume of the inorganic particles in a hybrid electrolyte is *p*:

$$V_{np} = p \qquad (2)$$

The volumetric distribution of the polymer (Vp) and interphase region (Vi) can calculated by:

$$V_p = (1-p)^{\eta^d}$$

$$V_i = 1 - p - (1-p)^{\eta^d}$$

where *d* represents the model dimensions (*d=3*). The overall ionic conductivity for the hybrid electrolyte can be calculated:

$$\sigma = \frac{\sigma_p\left[-A + \sqrt{A^2 + 2\tau(z-2-zV_{np})}\right]}{z-2} \qquad (3)$$

where,

$$A = \left[1 - \frac{zV_p}{2}\right] + \tau\left[1 - \frac{zV_i}{2}\right] \qquad (4)$$

and

$$\tau = \frac{\sigma_i}{\sigma_p}$$

Where sp is the ionic conductivity of the organic phase taken as 2x10-6 S cm-1 and si is the ionic conductivity of the interphase region taken as 1.5x10□ 5 S cm□ 1. Here, z is the coordination number (55) which is approximated from the percolation thresh- old pc = (z□ 2)=z which is assumed to be 0.96 for nano Al-LLZO.

4 Results and Discussion

4.1 Transport Properties

There are two percolation thresholds that exist in hybrid solid electrolytes: (1) long-range connectivity of inorganic particles (contact mode) (**Fig.**1**a**), and long-range connectivity of an interfacial layer (**Fig.**1**b**). The interfacial region describes the material properties of the polymer in direct contact with the inorganic particle (Al-LLZO). At the interface, a range of properties can be observed depending on chain orientation and confinement effects 35,36. Thus, this layer displays properties that are neither characteristic of the bulk polymer nor the bulk inorganic particle. This region is estimated to extend 2-3_ beyond the diameter of the inorganic particle 37,38. Contact percolation occurs at high loadings

of 33 vol% (ceramic:polymer) and the interfacial percolation can occur at _ 4 vol% (ceramic:polymer). However, these loadings are under the assumption that the particles are uniformly distributed with little or no agglomeration in the polymer matrix (i.e. electrolyte). Theoretically, if the highly conducting LLZO phase was fully percolated, lithium would transport through the inorganic material. However, in practice this does not occur and an order of magnitude decrease in ionic conductivity is observed when the inorganic content increases from 25 vol% (around percolation) to 50 vol% (above percolation) across all temperatures (25-70°C) (**Fig.**1**b**). Hybrid electrolytes that contain Al-LLZO concentrations around 5 and 25 vol% demonstrate similar behaviors in terms of ionic conductivity. Both electrolytes exhibit a conductivity around 2.0x10-6 Scm-1 at room temperature and about 3.0x10-4 Scm-1 at 70°C. The temperature dependent ionic conductivity (Arrhenius plot) is non-linear around the melting temperature for polyethylene oxide (60°C). This is due to the crystallization of polyethylene oxide below this point. The Arrhenius relation:

$$\sigma = \sigma_0 exp(-E_a/kT) \qquad (5)$$

is employed to estimate the activation energy for each electrolyte, where s0 is the pre-exponential factor, E_a is the activation energy, k is the Boltzmann constant (8.617x 10-5 ev K-1) and T is the temperature. Below 60°C the activation energy is > 0.40 eV for all samples except the 50 vol% which is ~ 0.37 eV. All hybrid electrolytes experience a decrease in the activation energy above the melting temperature of polyethylene oxide (Table 1).

The Al-LLZO content significantly affects the transport properties in a hybrid electrolyte (**Fig.**1**c**). The polyethylene oxide region of the hybrid electrolyte contains both anions (ClO_4^-) and cations (Li+) whereas the Al-LLZO region only carries charge via a lithium cation (i.e. single ion conductor)[39–41]. Thus, as the Al-LLZO concentration increases from 5 vol% to 50 vol% there is a subsequent increase in the transference number from 0.13 to 0.38 (Table 1). Addition of inorganic particles increases the Lewis acid type interactions as well as decreases the crystallinity of the polymer matrix. Lewis acid interactions between the chemical moieties on the inorganic particle surface and the anion and/or the polyethylene oxide restrict anion mobility as well as decrease Li+ interactions with O in the PEO matrix7. Polymer matrix crystallinity also reduces as the solid loading is increased leading to an enhancement of the ion transport properties and effective salt dissociation 42. These factors lead to the increase in transference number of the hybrid electrolytes. The presence of LLZO in the PEO matrix is clearly distinguishable from XRD patterns (Fig. S1a). As the ceramic loading gradually increases, intensity of the highly crystalline LLZO peaks susbtantially grows, suppressing the influence of polymer in the matrix. The Al-LLZO content also influences the ionic conductivity. As the Al-LLZO is increased from 5 to 15 vol% there is an increase in ionic conductivity and then above 15 vol% the ionic conductivity decreases. This trend is more pronounced at high temperatures (70°C). Prior work suggests that the improved transport is related to a decrease in polymer crystallinity with the addition of a filler material[8,10,42]. At high temperatures, above and around the melting point (Tm=60°C), the polymer will naturally reside in an amorphous form and thus the improved transport cannot completely be described by polymer physics (structure). It is challenging to probe the surface and bulk properties of the Al-LLZO particles because they are sub-surface and encapsulated in a polymer matrix. Typically, hybrid solid electrolytes are processed via the formation of a colloidal ink following by some sort of tape casting method (Fig. 2a). Thus, electrolytes can be coated into thin films and are free standing for use (Fig. 2b,c). During the preparation and processing of the colloidal ink, particles can aggregate and form a variety of structures [43,44]. The abnormality in aggregation due to higher loading can affect the properties of PEO-LLZO as a composite. Morphological differences in PEO-LLZO surface can be seen clearly with optical microscopy. The electrolyte surface morphology differs depending

on the composition. At low concentration (5 vol %) the morphology demonstrates some indication of phase separation and aggregation of the particles (Fig. 2d). As the sample loading is increased from 15 vol% and 50 vol%, the electrolyte becomes opaque taking on the coloring of the Al-LLZO nanoparticles. At these vol% loadings, little to no insight into structural properties can be discerned with standard imaging techniques. It is challenging to discern the underlying microstructure using standard surface visualization techniques. Rigorous structural analysis of the hybrid electrolytes with varying inorganic content is necessary to discern whether the improved transport is related to the bulk or surface properties of the Al-LLZO nanoparticles.

4.2 Quantitative 3D mophological analysis using nanotomography

Micro- and nano- X-ray computed tomography (XCT) is widely used to build a three dimensional understanding of a material's micro- and nano-structure. Technique resolution and quality is dependent on the specific optical set-up, but micro- computed tomography can achieve resolutions around 1mm and nanocomputed tomography can achieve resolutions around 60-100 nm (at synchrotrons). The trade-off between the techniques is field of view and resolution. The synthesized inorganic Al-LLZO has an average particle size of 200-300 nm (Fig. S3a) and thus falls outside the resolution limit of micro-tomography but is within the resolution limit of nano-computed tomography. The principle of nano-CT is demonstrated in Figure 2b. A series of 2D images are taken while the sample holder rotates from 0° to 180° (**Fig.**2**g**). The 2D images of the hybrid electrolytes demonstrate large attenuation contrast between the polymer and inorganic region (Al-LLZO). The polymer does not attenuate the x-rays and thus is transparent, leaving behind direct visualization of the Al-LLZO percolating networks (**Fig.** 2**g**). These images are subsequently binarized for quantitative analysis. The fraction of X-ray transparent region in the sample is computed using the pore size distribution package of ImageJ. Spheres of different radii are fit in the binarized domain for the X-ray transparent phase (dark region of binarized image, (**Fig.**3**a**). The volume of the total spheres fit in the domain gives us the fraction of that phase while the size distribution of sphere radii give the dimensions of the X-ray transparent phase. This geometric analysis was completed on various sub-volumes from 5 to 20 mm3 to identify a representative sub-volume for quantitative analysis (**Fig.**2**h**). Identification of a representative volume is essential for reliable quantification of results from tomography measurements22. Smaller sub-volumes can demonstrate anomalous local behavior that is not representative of the whole sample (Fig. S3a). On the other hand, larger sub-volumes visually provide more perspectives. But this comes along with X-ray influenced artifact containing regions, which is also not suitable for analyzing the heterogeneity of the system45. Moreover, it is computationally intense to do analysis on large sub-volumes. X-Ray transparent region fraction reaches a plateau value for all the loadings imaged at 15 mm^3 sub-volume dimension. This dimension was used for all subsequent quantitative analysis. In order to discern whether the Al-LLZO nanoparticles's surface or bulk properties are responsible for the improved transport properties, we set out to quantify the accessible surface area of the inorganic materials within the polymer matrix. In theory, the accessible surface area should increase as the Al-LLZO nanoparticles decrease in size and increase in concentration in a hybrid electrolyte. However, if any aggregation occurs this surface area will become inaccessible. Aggregation can be clearly observed when looking at a stack of binarized 2D images of the 5 vol% electrolyte at different z-heights (Fig. 3a). In the binarized images, the black region signifies the polymer region and the white region is representative of LLZO. We observe significant structural (surface area) heterogeneity in the electrolyte as we work our way up the z-axis (**Fig.** 3**b**). Figure 3b demonstrates the ratio of the white area to black (i.e. ceramic to polymer) for each z-height in the sub-volume. As the Al-LLZO content increases from 5 vol% to 50 vol% there is a ~3-10 x increase in accessible interfacial area. However, it should be noted that within 15 to 50 vol% the area increases by ~2% only. This contradicts the theoretical surface area estimation of this hybrid

systems which show that surface area for mono-dispersed particles should increase by ~3x on increasing the loading from 15 % to 50 %. This clearly signifies that there is severe particle agglomeration at higher loading forming continuous clusters within the hybrid electrolytes. To assess the degree of aggregation, we sorted out 10 largest connected clusters
for 5, 15 and 50 vol% (Fig. 3c). These are identified by tracking individual voxel neighbours in a sub-volume. Voxels with 26 neighbouring voxels in identical phase are considered as a part of a single cluster. Agglomeration effects are evident in these images where the largest cluster (yellow) is seen to almost take up the entire domain for 50 % sample. To aid visualization, three largest clusters for these loading are imaged separately (**Fig.** 3**d**). 5 vol% sample shows a uniform distribution of similar sized clusters. 15 vol% sample shows some degree of agglomeration as the cluster size is larger than those seen for 5 vol%. The three largest clusters are of similar size within the sample. However, for 50 vol% the largest cluster occupies the largest of the particle volume (324 mm^3), followed by clusters even smaller than what is for 5 vol% (Fig S3b). This is a direct evidence of agglomeration within the system which leads to a significant loss in accessible surface area of the particles. A complete reconstruction of the structural arrangement for different hybrid electrolytes from 5 to 50 vol% is shown in Figure 4. Accessible particle surface area was quantified by calculating the particle surface area to volume ratio of all samples (Fig.5). Surface area of the particles is estimated from the binarized images and normalized to the volume of particles in each sample. At low loading, the particle clusters are dispersed allowing complete access to the surface area. A large portion of the total particle surface area is lost as the Al-LLZO content is increased do the aggregation of the particles. The maximum normalized surface area is observed at 15 vol.% which is correlated to the highest ionic conductivity. This surface area relationships corroborates the proposed surface-driven transport hypothesis.

4.3 Percolation Model

The proposed surface-driven transport hypothesis is further corroborated via analysis of continuum percolation model. This model provides a simple yet reliable estimation of static interfacial properties that emerges from the interactions of nanoscale particles dispersed in polymer matrix. The formation of interphase due to particle-polymer interactions is expected to lead to a region with higher ionic conductivity than neat PEO (sp = 2x10-6 S cm-1). Although the interphase thickness l is influenced by particle loading, especially at higher volume fraction where overlapping interfaces are likely, it is appropriate to assume the thickness to be 2-3 times larger than the particle size 46. Figure 5 shows the relationship between Al-LLZO volume fraction (ϕ) and ionic conductivity and accessible surface area. The model (dashed line) matches the experimentally (squares) measured surface areas at low volume fractions fairly well but deviates significantly above 20 vol%. The percolation theory assumes a uniform distribution of particles, where in reality agglomeration sets in at even low vol%. Thus, due to agglomeration, the degree of percolation is reduced as well as the accessible surface area (Fig. 5).

Conclusions

Hybrid solid electrolytes combine a polymer ion conductor with an inorganic ion conductor in order to produce thin, flexible, and mechanically strong electrolytes for all solid state batteries. The addition of the secondary ion conducting phase (inorganic Al-LLZO) leads to enhanced transport performance at a composition of 15 vol% Al-LLZO. While there is a significant body of literature that ascribes this improvement to a decrease in the crystallinity in the polymer phase, this does not account for the enhanced performance seen above the melting temperature (Tm=650°C). Herein, we show that this enhancement is not a result of the bulk properties of the Al-LLZO, but instead is attributed to the polymerjparticle interaction. Nano-computed tomography is a effective tool for probing structural properties in hybrid electrolytes and reveals a direct relationship between inorganic accessible surface area and ionic conductivity. Furthermore, the increase in transferrence number at high Al-LLZO

content (and low ion conductivity) suggests that the Al-LLZO may form hydrogen bonding with the mobile anion, thereby limiting its charge-carrying ability. Future electrolyte designs and processing techniques that enable uniform particle distribution could enable highly conducting hybrid electrolytes.

6 Acknowedgements
The authors were supported by the National Science Foundation under grant No. 1847029. The authors acknowledge the Vanderbilt Institute of Nanoscience and Engineering (VINSE) for access to their shared characterization facilities. This research used resources of the Advanced Photon Source, a U.S. Department of Energy (DOE) Office of Science User Facility operated for the DOE Office of Science by Argonne National Laboratory under Contract No. DE-AC02-06CH11357.

References
1 J. Janek and W. G. Zeier, *Energy*, 2016, **500**, 300.
2 A. Manthiram, X. Yu and S. Wang, *Nature Reviews Materials*, 2017, **2**, 16103.
3 F. Shen, M. B. Dixit, X. Xiao and K. B. Hatzell, *ACS Energy Letters*, 2018, **3**, 1056–1061.
4 D. R. MacFarlane, J. Huang and M. Forsyth, *Nature*, 1999, **402**, 792.
5 N. Kamaya, K. Homma, Y. Yamakawa, M. Hirayama, R. Kanno, M. Yonemura, T. Kamiyama, Y. Kato, S. Hama, K. Kawamoto *et al.*, *Nature materials*, 2011, **10**, 682.
6 J. Li, C. Ma, M. Chi, C. Liang and N. J. Dudney, *Advanced Energy Materials*, 2015, **5**, 1401408.
7 F. Croce, G. Appetecchi, L. Persi and B. Scrosati, *Nature*, 1998, **394**, 456.
8 J. Zheng and Y.-Y. Hu, *ACS applied materials & interfaces*, 2018, **10**, 4113–4120.
9 J. Zheng, M. Tang and Y.-Y. Hu, *Angewandte Chemie International Edition*, 2016, **55**, 12538–12542.
10 X. C. Chen, X. Liu, A. Samuthira Pandian, K. Lou, F. M. Delnick and N. J. Dudney, *ACS Energy Letters*, 2019, **4**, 1080–1085.
11 B. Scrosati, *The Chemical Record*, 2001, **1**, 173–181.
12 Z. Zhang, S. Chen, J. Yang, J. Wang, L. Yao, X. Yao, P. Cui and X. Xu, *ACS applied materials & interfaces*, 2018, **10**, 2556–2565.
13 I. Gurevitch, R. Buonsanti, A. A. Teran, B. Gludovatz, R. O. Ritchie, J. Cabana and N. P. Balsara, *Journal of The Electrochemical Society*, 2013, **160**, A1611–A1617.
14 D. Devaux, K. J. Harry, D. Y. Parkinson, R. Yuan, D. T. Hallinan, A. A. MacDowell and N. P. Balsara, *Journal of The Electrochemical Society*, 2015, **162**, A1301–A1309.
15 I. Villaluenga, K. H. Wujcik, W. Tong, D. Devaux, D. H. Wong, J. M. DeSimone and N. P. Balsara, *Proceedings of the National Academy of Sciences*, 2016, **113**, 52–57.
16 W. Krawiec, L. Scanlon Jr, J. Fellner, R. Vaia, S. Vasudevan and E. Giannelis, *Journal of Power Sources*, 1995, **54**, 310–315.
17 Y. Lu, S. K. Das, S. S. Moganty and L. A. Archer, *Advanced Materials*, 2012, **24**, 4430–4435.
18 J. L. Schaefer, S. S. Moganty, D. A. Yanga and L. A. Archer, *Journal of Materials Chemistry*, 2011, **21**, 10094–10101.
19 A. S. Pandian, X. C. Chen, J. Chen, B. S. Lokitz, R. E. Ruther, G. Yang, K. Lou, J. Nanda, F. M. Delnick and N. J. Dudney, *Journal of Power Sources*, 2018, **390**, 153–164.
20 A. M. Stephan and K. Nahm, *Polymer*, 2006, **47**, 5952–5964.
21 D. Moreno, Y. Bootwala, W.-Y. Tsai, Q. Gao, F. Shen, N. Balke, K. B. Hatzell and M. C. Hatzell, *Environmental Science & Technology Letters*, 2018, **5**, 745–749.
22 M. B. Dixit, M. Regala, F. Shen, X. Xiao and K. B. Hatzell, *ACS Applied Materials & Interfaces*, 2018, **11**, 2022–2030.
23 W. E. Tenhaeff, X. Yu, K. Hong, K. A. Perry and N. J. Dudney, *Journal of the Electrochemical Society*, 2011, **158**, A1143–A1149.

24 Y. Li, W. Zhang, Q. Dou, K. W. Wong and K. M. Ng, *Journal of Materials Chemistry A*, 2019, **7**, 3391–3398.
25 J. Zheng, P. Wang, H. Liu and Y. Hu, *ACS Applied Energy Materials*, 2019.
26 W. Wang, E. Yi, A. J. Fici, R. M. Laine and J. Kieffer, *The Journal of Physical Chemistry C*, 2017, **121**, 2563–2573.
27 V. De Andrade, F. De Carlo, D. Gürsoy, D. Shu, A. Deriy, M. J. Wojcik and K. Fezzaa, *SPIE Newsroom*, 2016, DOI:10.1117/2.1201604.006461.
28 W. J. Palenstijn, K. J. Batenburg and J. Sijbers, *Journal of Structural Biology*, 2011, **176**, 250–253.
29 W. van Aarle, W. J. Palenstijn, J. De Beenhouwer, T. Altantzis, S. Bals, K. J. Batenburg and J. Sijbers, *Ultramicroscopy*, 2015, **157**, 35–47.
30 D. Gürsoy, F. De Carlo, X. Xiao and C. Jacobsen, *J. Synchrotron Radiat.*, 2014, **21**, 1188–1193.
31 C. A. Schneider, W. S. Rasband and K. W. Eliceiri, *Nature Methods*, 2012, **9**, 671–675.
32 H. E. Roman, *Journal of Physics: Condensed Matter*, 1990, **2**, 3909.
33 J. Bae, Y. Li, J. Zhang, X. Zhou, F. Zhao, Y. Shi and J. B. Goodenough, 2018, **78712**, 2096–2100.
34 N. J. DUDNEY, *Journal of the American Ceramic Society*, 1985, **68**, 538–545.
35 L. M. Hamming, R. Qiao, P. B. Messersmith and L. C. Brinson, *Composites science and technology*, 2009, **69**, 1880–1886.
36 M. T. Sebastian and H. Jantunen, *International Journal of Applied Ceramic Technology*, 2010, **7**, 415–434.
37 R. Qiao, H. Deng, K. W. Putz and L. C. Brinson, *Journal of Polymer Science Part B: Polymer Physics*, 2011, **49**, 740–748.
38 P. Tzika, M. Boyce and D. Parks, *Journal of the Mechanics and Physics of Solids*, 2000, **48**, 1893–1929.
39 Y. Tominaga and K. Yamazaki, *Chemical communications*, 2014, **50**, 4448–4450.
40 M. Armand, *Solid State Ionics*, 1983, **9**, 745–754.
41 Y. Tominaga, K. Yamazaki and V. Nanthana, *Journal of the Electrochemical Society*, 2015, **162**, A3133–A3136.
42 S. B. Aziz, T. J. Woo, M. F. Kadir and H. M. Ahmed, *Journal of Science: Advanced Materials and Devices*, 2018, **3**, 1–17.
43 K. B. Hatzell, M. B. Dixit, S. A. Berlinger and A. Z. Weber, *Journal of Materials Chemistry A*, 2017, **5**, 20527–0533.
44 M. B. Dixit, B. A. Harkey, F. Shen and K. B. Hatzell, *Journal of The Electrochemical Society*, 2018, **165**, F264–F271.
45 S. A. Vaselabadi, D. Shakarisaz, P. Ruchhoeft, J. Strzalka and G. E. Stein, *Journal of Polymer Science, Part B: Polymer Physics*, 2016, **54**, 1074–1086.
46 R. Qiao, H. Deng, K. W. Putz and L. C. Brinson, 2011, 740–748.

Fig. 1 Schematic of percolation regimes that exist in hybrid electrolytes (a) and ionic conductivity measurements for hybrid electrolytes with varying concentrations of inorganic (LLZO) fillers (b). Ionic conductivity represented as a function of volume fraction to highlight temperature dependent optimum (c).

Fig. 2 Hybrid electrolytes are typical solution processed (a) into free standing films of varying thickness (b,c). Optical images demonstrating the surface morphology of a hybrid electrolyte composed of 5 vol% (d), 15 vol% (e) and 50 vol% (f). A schematic of a how the inorganic microstructure can be extracted using synchrotron nano tomography (g). A geometric analysis on 3-D reconstructions to determine best volume (15 x15 x 15 mm^3 for quantitative analysis of reconstructed samples (h).

Fig. 3 Stack of binarized images demonstrate polymer and ceramic region in a hybrid electrolyte (a). The normalized ceramic area at different cross-sections in hybrid electrolytes containing 5, 15, and 50 vol% Al-

LLZO (b). The ten largest percolated (aggregated) structures in a sub-volume for 5, 15, and 50 vol% Al-LLZO (c) and exploded view of top three aggregated structures in each electrolyte (d).

Fig. 4 Reconstructed images for 5, 10, 15, 25 and 50 vol%

Fig. 5 :Theoretical (percolation theory), experimentally measured normalized surface area (sychrotron nano-CT) and experimentally
measured ionic conductivity.

Table 1 Activation energy and transference number for hybrid electrolytes

Figure 1

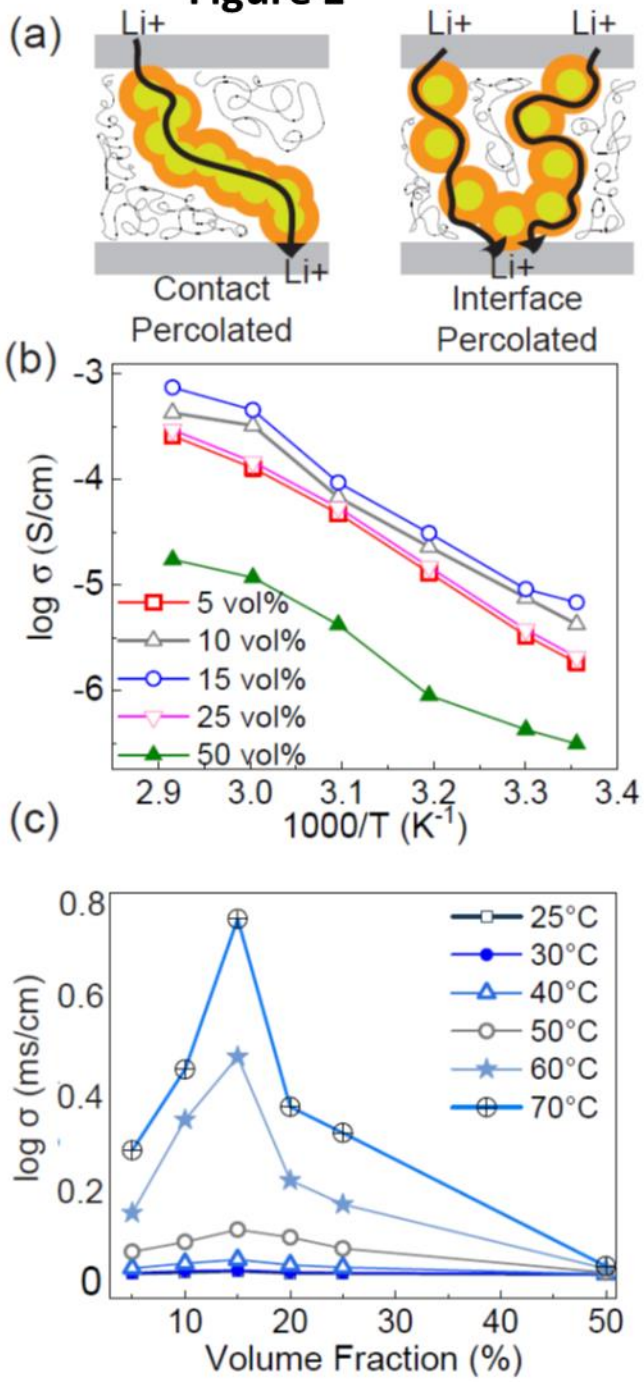
(a)
Li+
Li+
Li+
Li+
Contact Percolated
Interface Percolated
(b)
log σ (S/cm)
-3
-4
-5
-6
5 vol%
10 vol%
15 vol%
25 vol%
50 vol%
2.9
3.0
3.1
3.2
3.3
3.4
1000/T (K-1)
(c)
log σ (ms/cm)
0.8
0.6
0.4
0.2
0
25°C
30°C
40°C
50°C
60°C
70°C
10
20
30
40
50
Volume Fraction (%)

Figure 2

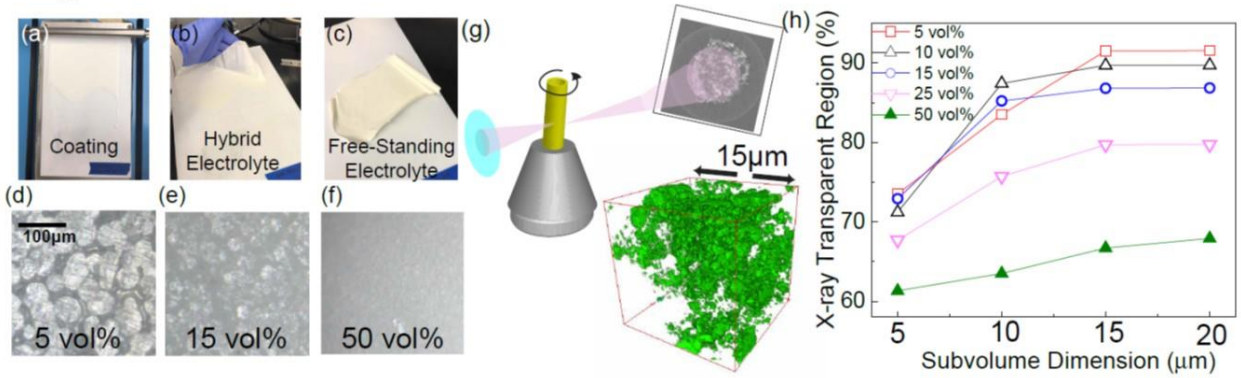

Figure 3

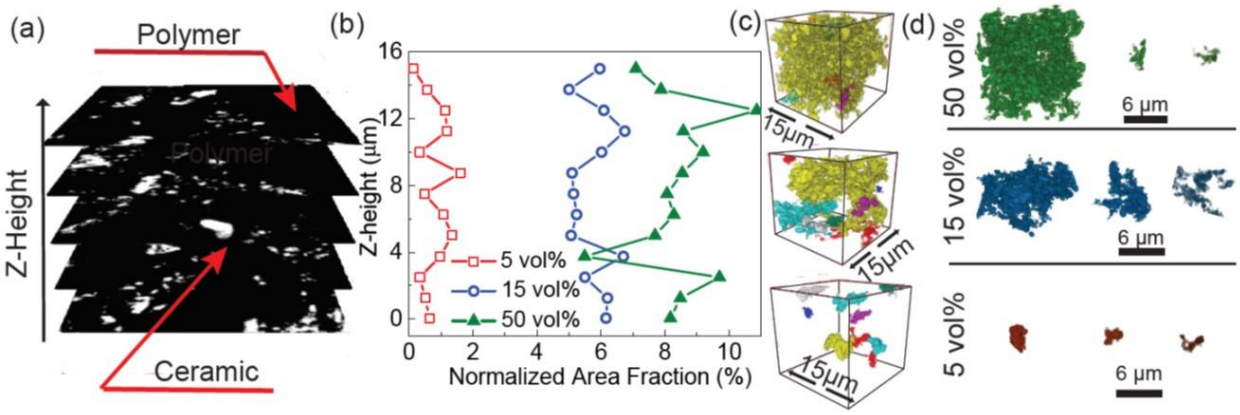

Figure 4

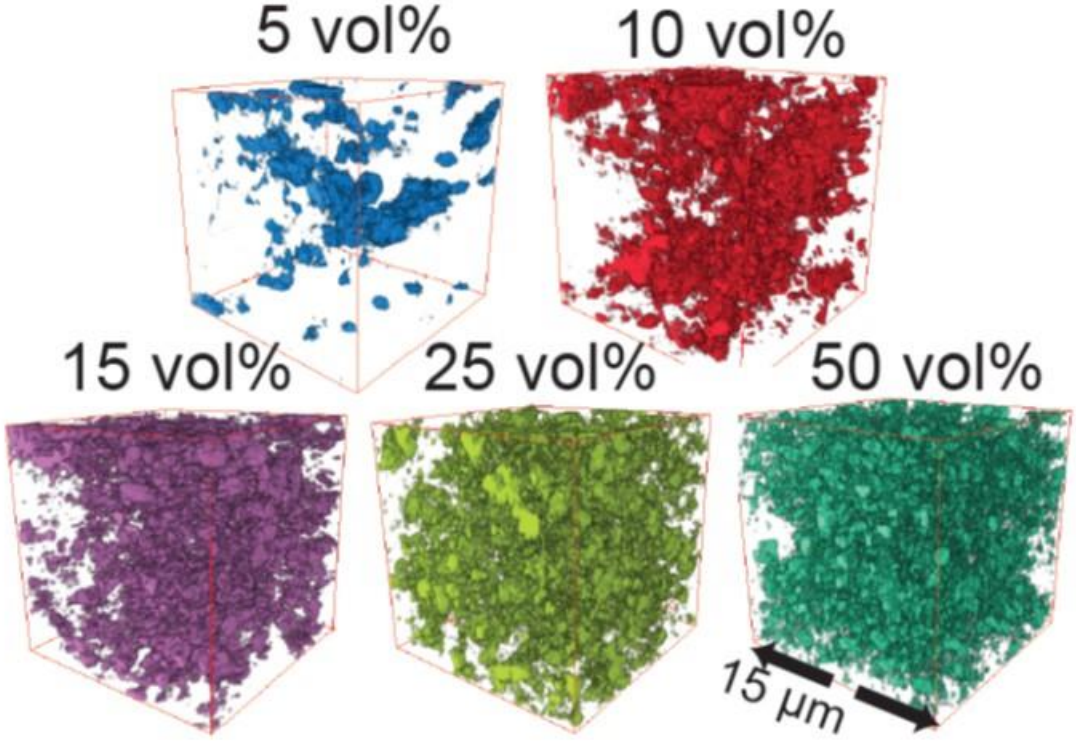

Figure 5

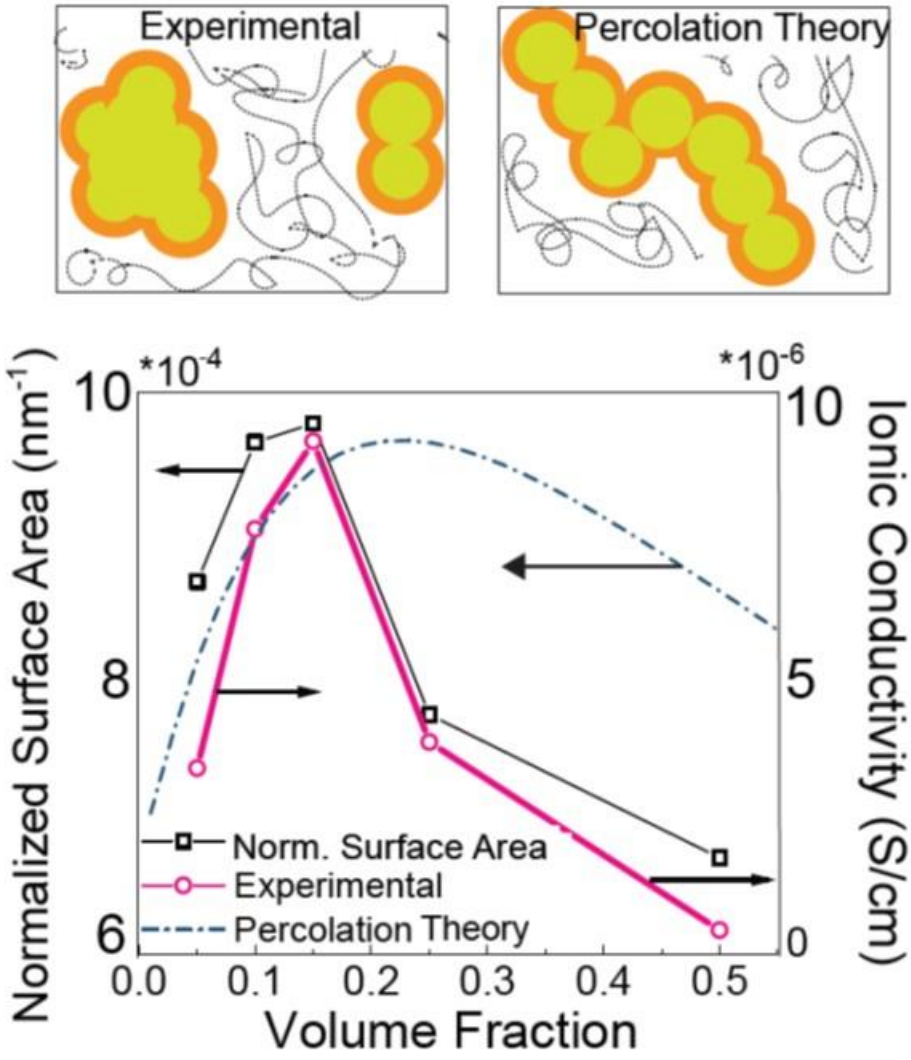

Table 1

Ceramic vol%	$E_a(eV)(<T_g)$	$E_a(eV)(>T_g)$	TN
5	0.47	0.35	0.13±0.02
10	0.40	0.39	0.22±0.03
15	0.46	0.34	0.24±0.02
25	0.47	0.35	0.28±0.04
50	0.37	0.30	0.38±0.03